Dual-axis versus Single-axis Excited Constant and Variable Speed Electric Generator and Synchronous Condenser Systems: A Review with Perspective

Ion Boldea, *Fellow, IEEE,* Adrian Daniel Martin, *Member, IEEE,* and Lucian Tutelea, *Member, IEEE*

***Abstract*—Modern/distributed electric energy systems, with ever larger penetration of renewable (photovoltaic, wind, wave, and hydro) energy sources and time-variable outputs, are in need of stronger/higher frequency and alternating current (AC) (direct current (DC)) voltage control. In fact, faster and more stable active and reactive power in the presence of frequency and voltage sags and swells is needed. Power electronics-controlled variable speed generators do not have enough energy storage (inertia) for the scope (static synchronous compensators (STATCOMs) included). This is because power electronics tends to decouple the generator from the power system. While virtual inertia control in doubly fed induction generators (DFIGs) offers a partial solution to these problems, a more robust and comprehensive framework is required for advanced grid support. This is how, by extending the dual-excitation principles, the dual-axis excited electric synchronous generators (DE-SG) provide superior flexibility in two variants summarized here: as a multifunctional DFIG and dual-axis vs. single-axis excited synchronous generator (SG), and as a synchronous condenser (SC), with dual DC and AC excitation (as a no-load DFIG with inertia wheel), where variable speed is used to accelerate/ decelerate the SC and thus provide additional assistance in frequency stabilization. These solutions, good for short-time transients, are not meant, however, to replace the large bidirectional energy storage systems (pump-hydro, hydrogen, batteries, etc.) which are crucial for the daily inherent variations of output energy in modern power systems with multiple power sources. The present paper offers a summary of techniques used in the dual-axis excited vs. single-axis excited SGs (SE-SGs), and SCs topologies, modeling, and control for better stability in modern multiple-source energy systems. This survey includes multiple case studies to shed light on prominent methods.**

***Index Terms*—Doubly fed induction generators (DFIG), Dual-axis excited electric synchronous generator (DE-SG), Dual-axis excited electric synchronous condenser (DE-SC), Grid stability, Virtual inertia.**

I. INTRODUCTION

TRADITIONALLY, alternating current (AC) energy systems use constant speed (frequency) single direct current (DC) excited synchronous generators in parallel, with complex, 4-level, sophisticated controls to tightly regulate them for constant frequency and AC voltage amplitude, during input and output power inherent variations.

So far, single DC-excited synchronous generators (SGs) have been able to match input and output power within a fraction of a second, but this requires adequate control and a temporary reduction of consumption for sacrificed consumers.

II. THE SINGLE-EXCITED SYNCHRONOUS CONDENSER (SE-SC)

The classical combined control of single-DC-excited SGs for constant frequency output in standalone power systems consists mainly of 1) DC excitation control (proportional-integral-derivative (PID) control, sliding mode, etc.) for output voltage control commanded through a voltage droop vs. reactive power and 2) turbine generator speed control (whose structure depends on turbine type) commanded by the frequency slight but variable droop with active power demand increase.

Varying the two droops, the active and reactive power requirements of each generator may be changed, while all of them are in parallel in a regional or a national standalone power system at basically the same frequency, with a reduction/increase of around 0.3–0.5 Hz to avoid flicker and loss of stability of the system.

The main merits of single-dc-excited SG regulated at rather constant output voltage and speed are the rotor cage attenuation of speed (power) oscillations in case of load variations, and the inertia of the SG + turbine participation at generator stability during load transients or faults. The need for better performance during power system transients, with the necessity of more pump-storage to level variable energy consumption during the day, led recently to the development and deployment of the first 100–200 MVA variable speed single DC excited SG with full power rating back-to-back pulse-width modulation (PWM) modular multilevel converter. The high cost of such large power PWM converters and the "separation" of SG inertia from the power grid, as well as the SG inherent reactive power absorption limitation (by keeping

Manuscript received November 20, 2025; revised January 9, 2026 and February 3, 2026; accepted February 26, 2026. Date of publication March 25, 2026; Date of current version March 24, 2026.

Ion Boldea is with Romanian Academy, Timisoara Branch, Timișoara 300223, Romania (e-mail: ion.boldea@upt.ro).

Adrian Daniel Martin and Lucian Tutelea are with Department of Electrical Engineering Politehnnica University Timișoara, Timișoara 300223, Romania (e-mail: adrian.martin@upt.ro, lucian.tutelea@upt.ro).

(*Corresponding author: Adrian Daniel Martin)*

Digital Object Identifier 10.30941/CESTEMS.2026.00010

the field current still positive but small), which leads to stability issues, are the main challenges of this growing recent trend in sophisticated modern power systems. Besides, from the unusually rich literature on single DC excited SG control in power systems, we mention here only two recent investigations which seem to have a strong potential for industrial application:

1) The high temperature superconducting (HTS)-excitation SG [1]

In an effort to reduce the volume, weight, and cost of large SGs, while increasing their efficiency by about 1% and, especially, enhancing their reactive power absorption capability (due to their much smaller synchronous reactance in p.u.), these systems are vital during sudden large-scale photovoltaic (PV) or wind energy perturbations. Such capabilities help avoid voltage swells and, ultimately, prevent protection tripping.

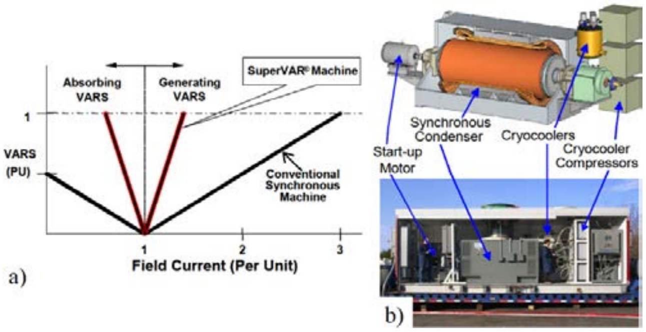

Fig. 1 (a) V-curves for conventional synchronous and HTS SC machines. (b) AMSC's +/− 8 MVAR HTS SC machine with key characteristics highlighted [1].

In principle, an HTS DC multipolar excitation, which produces, in the case of the typical SG, stator a flux density of about 2.0 + T, and thus reduces the machine size notably, while the synchronous reactance is of the order of 0.36 p.u. in a 10 MVA unit. A small variation of the HTS current (±10% around 350 A [1]) is enough to switch from delivered to absorbed reactive power of high p.u. However, this switching to large absorbed reactive power takes 100 s or so [1], which may be necessary to reduce the probability of quenching the HTS.

2) The series compensated SG/SC [2]-[3]

Another solution is to increase the reactive power exchange rating by using an SC (which is a synchronous motor with no load at the shaft). As proposed in [2]-[3], it consists of a permanent magnet (PM) synchronous machine with open-end stator winding connected to a transformer and then to a PWM dedicated converter. Fig. 2(b) clearly demonstrates the effectiveness of the series compensator in mitigating power oscillations and maintaining bus voltage stability. The solution may also be used in the design of such PM excited with series compensation SGs.

To extend the active-reactive power range of SGs, hybrid (PM + DC) single-axis excitation has been recently investigated [4] by using the lower computation effort of a nonlinear three-dimensional (3D) equivalent magnetic network. The loss of excitation fault in SGs produces an abrupt decrease in output active power (only the magnetic saliency power remains) and a sharp increase in absorbed reactive power, which warrants comprehensive investigation in [5].

The even higher penetration of time-variable renewable energy (especially from PV and wind sources), along with the ubiquitous use of power electronics, has practically "decoupled" the energy sources from the power systems in terms of frequency (speed) and voltage. Power electronics can quickly regulate the AC (or DC) output voltage, but

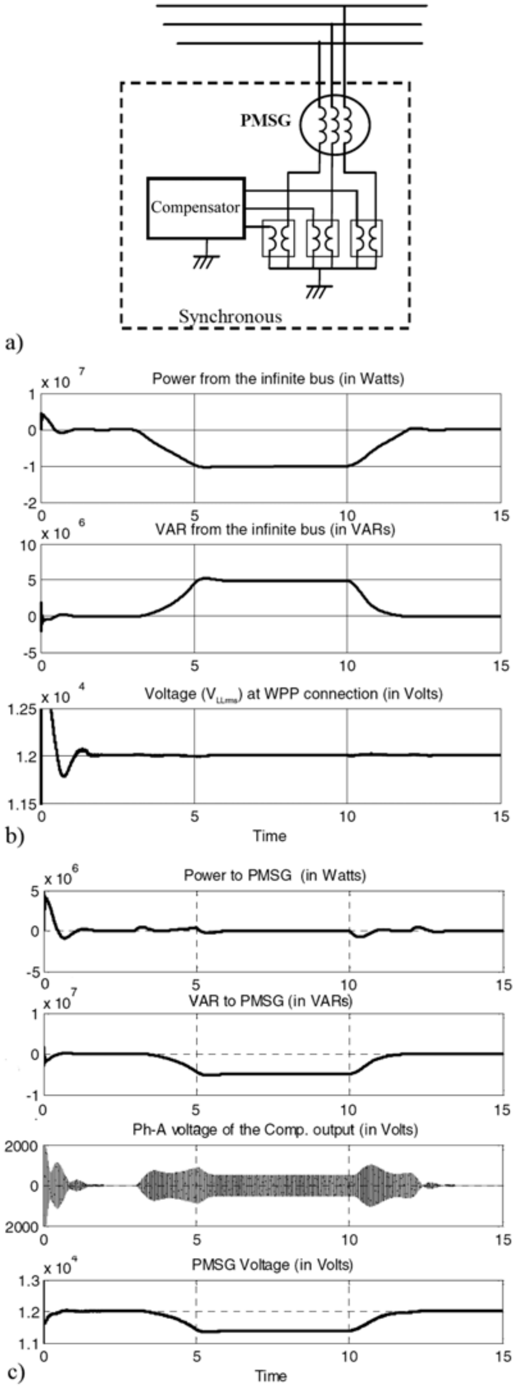

Fig. 2. (a) Configuration of the SC. (b) Power from the infinite bus, VAR from the finite bus, and the voltage at the WPP POI. (c) Power to the PMSG, VAR to the PMSG, phase-A output voltage of the compensator, and the line voltage of the PMSG [2].

adapt to variations in active power (load), energy storage is necessary. Today, in PVs, the only components available for energy storage are the DC-link capacitors (unless a large battery is connected to the DC link).

As a result, no mechanical inertia is directly available in such systems for fast frequency (active power) stabilization.

While static synchronous compensators (STATCOMs), by using a controlled rectifier with a DC capacitor link, may provide AC voltage (reactive power) control in the energy system, they lack inertia and can show instabilities when a large active power variation is involved in the power system [6].

In addition, the use of SCs offers a significant increase in the short-circuit ratio (SCR) compared to static VAR compensators (SVC). While both provide reactive power support, SVCs—also known as static VAR systems (SVSs)—differ fundamentally from STATCOMs. An SVC acts as a variable impedance using a combination of thyristor-controlled reactors and shunt capacitors, meaning its reactive power output is highly dependent on the square of the system voltage. In contrast, a STATCOM utilizes voltage sourced converter (VSC) technology, allowing it to behave as a controllable voltage source that provides superior performance during severe voltage drops and a faster dynamic response. In [7], the authors present simulation results comparing the SVC with the SC, demonstrating that the SC outperforms the SVC in terms of SCR enhancement and stability during fault conditions (Fig. 3).

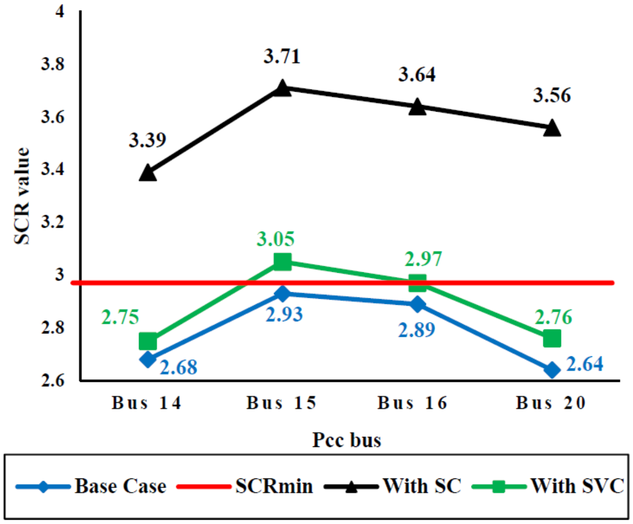

Fig. 3 Comparison of SCR for different simulation cases [7].

This is why the SC [8] (which is essentially a no-load synchronous motor) has been revived recently. But, in the present paper, a dq excitation to control AC voltage by d-axis excitation current (i_{df}), and torque by q-axis excitation current (i_{qf}) to provide SC stability even when i_{df} is small or even negative. To absorb more reactive power and reduce voltage swells from excess PV energy. To self-start the SC, the dq excitations may be fed AC by two single-phase power inverters.

In this mode, the SC operates similarly to a doubly fed induction generator (DFIG). it is fed in the rotor with the stator being short-circuited up to a predefined speed, after which the self-synchronization sequence is initiated. Tens of 300 MVA SC units have already been installed in China [9]. Even in variable-speed DFIGs and SGs, the inertia energy available for frequency stabilization is limited due to the presence of a dual AC-DC-AC PWM converter [10]-[17].

Another practical solution already presented in the literature is given in Fig. 4 by Siemens [18], where an SE-SC with a flywheel for increasing inertia is presented. Several solutions are already in operation: Robertstown, Australia (2x Turnkey SCs incl. Flywheel at 275 kV, 2021), Oberottmarshausen, Germany (1x SC, −200/+300 MVAR, at 400 kV, 2018), Moneypoint, Ireland (1x SC with flywheel-111/245 MVAR at 400 kV, 4000 MWs, 2023) [18].

Fig. 4 SE-SC, Siemens [18].

To better solve this problem, four solutions are analyzed in this paper, that can better handle both active and reactive power control in modern energy systems: the a SG for constant (Section III) and variable speed (Section IV), the dual-axis excited SC (Section V) already commercialized in [19], the DFIG multifunctional (MFG) system with reconfigurable control for constant and variable speed (Section IV).

The subsequent sections are dedicated to a comprehensive analysis of these technologies, structured as follows:

1) Section II: The SE-SC;
2) Section III: The dual-axis excited electric SG (DE-SG) for constant speed;
3) Section IV: The DE-SG for variable speed;
4) Section V: The dual-axis excited SC (DE-SC);
5) Section VI: The DFIG as an MFG system with reconfigurable control (proposed);
6) Section VII: DFIG with diode rectifier controlled output (a case study for MFG generator)

III. THE DUAL-AXIS EXCITED DE-SG FOR CONSTANT SPEED

As explained earlier, the larger renewable energy penetration in AC energy systems and the excess of reactive power in M(H)VDC power transmission systems have propelled the revival of a dual-axis excited SG in order to enhance dynamic performance and stability [20]-[21]. First introduced in the nineteen seventies, the dual-excitation synchronous generator was mainly intended for constant-speed applications, as power electronics was not advanced then [21]-[23]. As visible in Figs. 5(a) and 5(b), the DE-SG typically includes a 3-phase AC distributed winding in the stator, dq distributed excitations, and a damping winding on the rotor [9]. The two excitation windings may be asymmetric or symmetric Fig. 6.

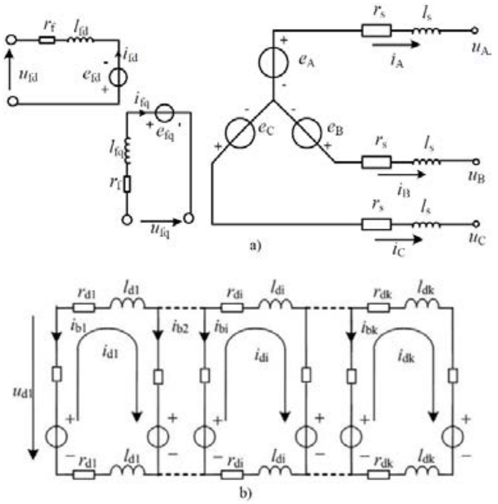

Fig. 5 DE-SG. (a) The dq excitation and stator 3-phase AC winding. (b) Rotor damping winding [9].

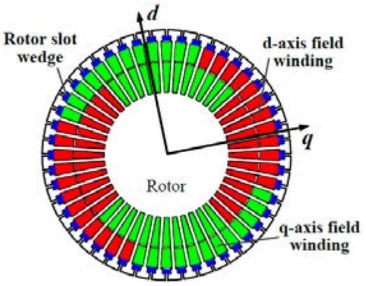

Fig. 6 Distributed d-q rotor excitation windings with slot conducting wedges (as a surrogate damper winding) [9].

The two-phase orthogonal rotor windings in the uniform slotted configuration shown in Fig. 6 are designed to be symmetric. Consequently, they behave similarly to three-phase symmetric windings, despite some differences in magneto-motive force (MMF) harmonics. For variable speed operation, these windings receive AC currents at slip frequency, making the rotor behavior analogous to that of a DFIG under vector control. If a speed variation of up to ±30% is targeted, the system adopts a DFIG-like behavior. However, a narrower speed range may be preferred to reduce the kVA rating of the rotor windings. Furthermore, the use of high-resistivity rotor slot wedges has proven effective in reducing peak excitation currents during voltage regulation. These components could be integrated into the DFIG equivalent of the DE-SG.

In general, DC two excitation windings are fed directly from ground sources through brushes and slip rings or by brushless systems.

A. DE-SG modeling

The modeling by 2D time-stepping finite element method (FEM) of such a machine [9] is based on a matrix equation:

$$\boldsymbol{K}\cdot\boldsymbol{A}-\boldsymbol{C}_{\mathrm{s}}\cdot\boldsymbol{I}_{\mathrm{s}}-\boldsymbol{C}_{\mathrm{fd}}\cdot\boldsymbol{i}_{\mathrm{fd}}-\boldsymbol{C}_{\mathrm{fq}}\cdot\boldsymbol{i}_{\mathrm{fq}}+\left(\boldsymbol{D}_{\mathrm{s}}+\boldsymbol{D}_{\mathrm{r}}\right)\cdot\frac{\mathrm{d}\boldsymbol{A}}{\mathrm{d}t}=0 \tag{1}$$

where $\boldsymbol{A}$ is the vector potential; $\boldsymbol{C}_{\mathrm{s}}$, $\boldsymbol{C}_{\mathrm{fd}}$, and $\boldsymbol{C}_{\mathrm{fq}}$ are coordination matrices of stator currents; $\boldsymbol{D}_{\mathrm{s}}$ and $\boldsymbol{D}_{\mathrm{r}}$ are the incidence matrices in relation to eddy currents in rotor slot wedges; $\boldsymbol{K}$ is the stiffness matrix in each FEM element; i_{fd} and i_{fq} and are the d-q axis field currents.

Based on (1), the voltage matrix equation is:

$$\bar{\boldsymbol{V}}_{\mathrm{l}}=\bar{\boldsymbol{E}}_{\mathrm{s}}-\boldsymbol{R}_{\mathrm{s}}\cdot\bar{\boldsymbol{I}}_{\mathrm{s}}-\boldsymbol{L}_{\mathrm{s}}\cdot\frac{\mathrm{d}\bar{\boldsymbol{I}}_{\mathrm{s}}}{\mathrm{d}t} \tag{2}$$

With $\bar{\boldsymbol{V}}_{\mathrm{l}}$ = $[v_{\mathrm{A}}, v_{\mathrm{B}}, v_{\mathrm{V}}]^{\mathrm{T}}$ and $\bar{\boldsymbol{I}}_{\mathrm{s}}$ = $[i_{\mathrm{A}}, i_{\mathrm{B}}, i_{\mathrm{C}}]^{\mathrm{T}}$ as the stator voltage and current; $\bar{\boldsymbol{E}}_{\mathrm{s}}$ = $[e_{\mathrm{A}}, e_{\mathrm{B}}, e_{\mathrm{C}}]^{\mathrm{T}}$ represents the total three-phase stator electromotive forces matrix; $\boldsymbol{R}_{\mathrm{s}}$ = diag$[r_{\mathrm{s}}, r_{\mathrm{s}}, r_{\mathrm{s}}]$ represents the diagonal matrix of the stator resistance; $\boldsymbol{L}_{\mathrm{s}}$ = diag$[l_{\mathrm{s}}, l_{\mathrm{s}}, l_{\mathrm{s}}]$ represents the diagonal matrix of the end leakage inductance of the stator winding.

Also [9]:

$$\begin{aligned} v_{\mathrm{fd}}&=-l_{\mathrm{ef}}\cdot\boldsymbol{C}_{\mathrm{fd}}^{\mathrm{T}}\frac{\mathrm{d}\boldsymbol{A}}{\mathrm{d}t}+r_{\mathrm{fd}}\cdot\boldsymbol{i}_{\mathrm{fd}}+l_{\mathrm{fd}}\frac{\mathrm{d}\boldsymbol{i}_{\mathrm{fd}}}{\mathrm{d}t}\\ v_{\mathrm{fq}}&=-l_{\mathrm{ef}}\cdot\boldsymbol{C}_{\mathrm{fq}}^{\mathrm{T}}\frac{\mathrm{d}\boldsymbol{A}}{\mathrm{d}t}+r_{\mathrm{fq}}\cdot\boldsymbol{i}_{\mathrm{fq}}+l_{\mathrm{fq}}\frac{\mathrm{d}\boldsymbol{i}_{\mathrm{fq}}}{\mathrm{d}t}\end{aligned} \tag{3}$$

where v_{fd} and v_{fq} are the dq-axis voltages of the field winding; l_{ef} represents the length of the rotor core; l_{fd} and l_{fq} represent the dq-axis field windings leakage inductances; r_{fd} and r_{fq} represent the dq-axis field windings resistances; $\boldsymbol{C}_{\mathrm{fd}}^{\mathrm{T}}$ and $\boldsymbol{C}_{\mathrm{fq}}^{\mathrm{T}}$ are the transposed correlation matrices of the stator current. For the two-field circuit equations, l_{ef} is the length of the rotor core. Finally, the rotor damping winding equations are [9]:

$$\begin{aligned}&\boldsymbol{H}_{\mathrm{d1}}\cdot\boldsymbol{U}_{\mathrm{d}}+\boldsymbol{G}_{\mathrm{ed}}\cdot\boldsymbol{I}_{\mathrm{d}}+\boldsymbol{H}_{\mathrm{d2}}\frac{\mathrm{d}\boldsymbol{A}}{\mathrm{d}t}=0\\ &\boldsymbol{G}_{\mathrm{ud}}\cdot\boldsymbol{U}_{\mathrm{d}}+\boldsymbol{R}_{\mathrm{d}}\cdot\boldsymbol{I}_{\mathrm{d}}+\boldsymbol{L}_{\mathrm{d}}\frac{\mathrm{d}\boldsymbol{i}_{\mathrm{d}}}{\mathrm{d}t}=0\end{aligned} \tag{4}$$

where $\boldsymbol{U}_{\mathrm{d}}=[u_{\mathrm{d1}}...u_{\mathrm{d}i}...u_{\mathrm{d}k}]^{\mathrm{T}}$, $\boldsymbol{I}_{\mathrm{d}}=[i_{\mathrm{d1}}...i_{\mathrm{d}i}...i_{\mathrm{d}k}]^{\mathrm{T}}$, $\boldsymbol{G}_{\mathrm{Id}}$, and $\boldsymbol{G}_{\mathrm{ud}}$ are the transfer matrices; $\boldsymbol{R}_{\mathrm{d}}=\mathrm{diag}[2\cdot r_{\mathrm{d1}},...,2\cdot r_{\mathrm{d}k}]$, $\boldsymbol{L}_{\mathrm{d}}=\mathrm{diag}[2\cdot l_{\mathrm{d1}},...,2\cdot l_{\mathrm{d}k}]$, $\boldsymbol{H}_{\mathrm{d1}}=\mathrm{diag}[\sigma_{\mathrm{S}}S/l_{\mathrm{ef}},...,\sigma_{\mathrm{S}}S/l_{\mathrm{ef}}]$, and $H_{\mathrm{d2}}^{\mathrm{e}}=-\sigma_{\mathrm{d}}\Delta_{\mathrm{e}}/3$.

With the damping winding circuit in axis d as in Fig. 5(b), (1)–(3) lead to the DE-SG voltage equations [9]:

$$\begin{gathered}\begin{bmatrix}\boldsymbol{D}_{\mathrm{s}}+\boldsymbol{D}_{\mathrm{r}} & 0 & 0 & 0 & 0 & 0\\ -l_{\mathrm{ef}}\boldsymbol{C}_{\mathrm{s}}^{\mathrm{T}} & -\boldsymbol{L}_{\mathrm{s}} & 0 & 0 & 0 & 0\\ -l_{\mathrm{ef}}\boldsymbol{C}_{\mathrm{fd}}^{\mathrm{T}} & 0 & l_{\mathrm{fd}} & 0 & 0 & 0\\ -l_{\mathrm{ef}}\boldsymbol{C}_{\mathrm{fq}}^{\mathrm{T}} & 0 & 0 & l_{\mathrm{fq}} & 0 & 0\\ \boldsymbol{H}_{\mathrm{d2}} & 0 & 0 & 0 & 0 & 0\\ 0 & 0 & 0 & 0 & 0 & L_{\mathrm{d}}\end{bmatrix}\frac{\mathrm{d}}{\mathrm{d}t}\begin{bmatrix}\boldsymbol{A}\\ \boldsymbol{I}_{s}\\ \boldsymbol{i}_{\mathrm{fd}}\\ \boldsymbol{i}_{\mathrm{fq}}\\ \boldsymbol{V}_{\mathrm{d}}\\ \boldsymbol{I}_{\mathrm{d}}\end{bmatrix}+\\ \begin{bmatrix}\boldsymbol{K} & -\boldsymbol{C}_{\mathrm{s}} & -\boldsymbol{C}_{\mathrm{fd}} & -\boldsymbol{C}_{\mathrm{fq}} & \boldsymbol{C}_{\mathrm{d}} & 0\\ 0 & -\boldsymbol{R}_{\mathrm{s}} & 0 & 0 & 0 & 0\\ 0 & 0 & r_{\mathrm{fd}} & 0 & 0 & 0\\ 0 & 0 & 0 & r_{\mathrm{fq}} & 0 & 0\\ 0 & 0 & 0 & 0 & \boldsymbol{H}_{\mathrm{d1}} & \boldsymbol{G}_{\mathrm{Id}}\\ 0 & 0 & 0 & 0 & \boldsymbol{G}_{\mathrm{Ud}} & \boldsymbol{R}_{\mathrm{d}}\end{bmatrix}\begin{bmatrix}\boldsymbol{A}\\ \boldsymbol{I}_{\mathrm{s}}\\ \boldsymbol{i}_{\mathrm{fd}}\\ \boldsymbol{i}_{\mathrm{fq}}\\ \boldsymbol{V}_{\mathrm{d}}\\ \boldsymbol{I}_{\mathrm{d}}\end{bmatrix}=\begin{bmatrix}0\\ \boldsymbol{V}_{\mathrm{l}}\\ \boldsymbol{v}_{\mathrm{fd}}\\ \boldsymbol{v}_{\mathrm{fq}}\\ 0\\ 0\end{bmatrix}\end{gathered} \tag{5}$$

To complete the model, the motion and torque equations are added based on [9]:

$$\begin{cases} J\cdot\dfrac{\mathrm{d}\omega}{\mathrm{d}t}=T_{\mathrm{L}}-T_{\mathrm{e}}; \quad \dfrac{\mathrm{d}\theta}{\mathrm{d}t}=\omega-\omega_0 \\ T_{\mathrm{e}}=\dfrac{r^2\cdot l_{\mathrm{ef}}}{\mu_0}\displaystyle\sum_{k=1}^{N_{\mathrm{e}}}\int_{\theta_k}^{\theta_{k+1}}\left(B_{kr}\cdot B_{k\theta}\right)\mathrm{d}\theta \end{cases} \tag{6}$$

This rather complex model has been proven adequate on a 10 kW lab prototype with equal excitation currents during a sudden short circuit, as in Fig. 7, as in [9]:

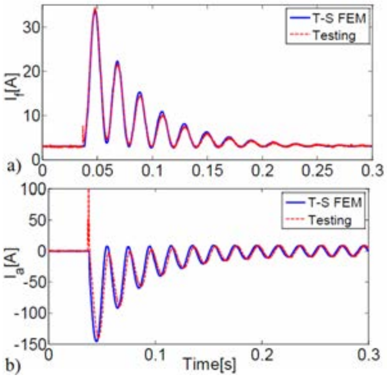

Fig. 7 Sudden short circuit of DE-SG. (a) Field current I_f. (b) Stator current i_a [9].

where ω and ω_0 represent the angular and synchronous speed of the DE-SG; T_L, T_e, and θ represent the loading torque of the prime mover, and the electromagnetic torque and the rotor angle of the DE-SG, respectively; B_{kr} and $B_{k\theta}$ represent the radial and tangential magnetic air gap flux densities of each FEM element; r represents the integral radius; N_e represents the number of triangular units; μ_0 is the air gap permeability; J represents the moment of inertia.

$$\begin{aligned} P&=3\cdot\frac{V_{\mathrm{s}}}{X_{\mathrm{s}}}\cdot\left(E_{\mathrm{q}}\cdot\sin\delta+E_{\mathrm{d}}\cdot\cos\delta\right)\\ Q&=3\cdot\left(\frac{V_{\mathrm{s}}\cdot E_{\mathrm{q}}}{X_{\mathrm{s}}}\cdot\cos\delta-\frac{V_{\mathrm{s}}\cdot E_{\mathrm{d}}}{X_{\mathrm{s}}}\cdot\sin\delta-\frac{V_{\mathrm{s}}^2}{X_{\mathrm{s}}}\right)\end{aligned} \tag{7}$$

In the absence of losses, the active and reactive powers P and Q are as above, corroborating simply the contributions of the two (d, q) excitation electromotive forces (EMFs) E_d and E_q, with X_s being the machine synchronous reactance and δ the power angle between the stator voltage (V_s) and resultant EMF.

B. Control options for DE-SG

Once the above model of the DE-SG was verified the control of it is illustrated here in two variants:

1) DE Control V_{fd}, V_{fq}

A proportional-only feedback of the active (ΔP) and reactive (ΔQ) powers, rotor speed ($\Delta\omega_r$), power angle ($\Delta\delta$) and field current (Δi_{fq}) is a first option [9]:

$$\begin{cases} V_{\mathrm{fq}}=V_{\mathrm{fq0}}+\dfrac{r_{\mathrm{fq}}}{x_{\mathrm{aq}}}\left(K_p\cdot\Delta P+K_\omega\cdot\Delta\omega+K_\delta\cdot\Delta\delta+K_{i_{\mathrm{f}}}\cdot\Delta i_{\mathrm{f}}\right)\\ V_{\mathrm{fd}}=V_{\mathrm{fd0}}+\dfrac{r_{\mathrm{fd}}}{x_{\mathrm{ad}}}\left(K_Q\cdot\Delta Q\right)\end{cases} \tag{8}$$

where V_{fq} and V_{fd} represent the dq-axis field voltages; V_{fq0} and V_{fd0} represent the dq-axis field voltages before disturbances; x_{ad} and x_{aq} represent the dq-axis armature reaction reactance; P and Q represent the active and reactive power; i_f represents the field current; $\Delta P = P - P_0$, $\Delta\omega = \omega - \omega_0$, $\Delta\delta = \delta - \delta_0$, $\Delta i_f = i_f - i_{f0}$, and $\Delta Q = Q - Q_0$ represent the feedbacks of the specific measurements; K_P, K_ω, K_δ, K_{i_f}, and K_Q are the gains for ΔP, $\Delta\omega$, $\Delta\delta$, Δi_f, and ΔQ.

2) Power Tracking Excitation Control (PTEC)

The block diagram of power tracking excitation control is shown in Fig. 8, from [9].

The three input errors $P - P_0$, $i_{fq} - i_{fd}$, $Q - Q_0$, and the V_{fq}, V_{fd} reference values are clearly visible in Fig. 8.

In large inertia systems, the proportional (K) control is not sufficient, and thus a simple improvement would be to add a first-order differential control ([9]) such that:

$$\frac{U(s)}{E(s)}=G(s)=K_{\mathrm{p}}+\frac{sM_{\mathrm{p}}}{1+sN_{\mathrm{p}}} \tag{9}$$

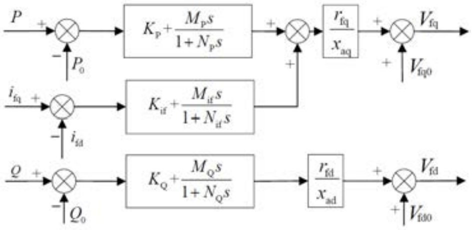

Fig. 8 Block diagram of power tracking excitation control [9].

where U and E represent the output and the input variable, K_p, M_p, and N_p are the proportional, differential, and inertia coefficients, respectively, and s represents the Laplace operator.

In discreet time, from [9]:

$$v(k)=K\cdot e(k)+\frac{M(1-a)\big(e(k)-e(k)\big)}{\Delta t}\cdot av(k-1) \tag{10}$$

Here $0<a=\dfrac{N}{N+\Delta t}<1$, with Δt the sampling period. k represents the number of samples, e represents the error, K represents the proportional coefficient, and v represents the output variable.

For a 300 MVA DE-SG unit, simulation results for torque and, respectively, reactive power disturbance show clearly the superiority of power tracking excitation control (Fig. 9) in terms of speed max. error and settling time.

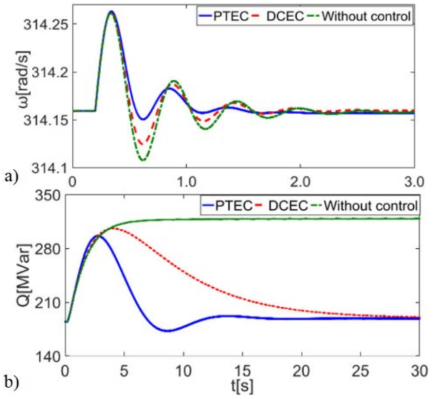

Fig. 9 DE-SG response for a 300 MVA unit. (a) To torque perturbation in speed. (b) To reactive power disturbance [9].

The model described above was also applied to calculate the transient parameters of DE-SG [24], while the influence of rotor damping winding material on the DE-SG transients is treated in [25] with parameter optimization, to reduce frequency fluctuation amplitude and oscillation duration in speed.

Other recent advanced investigations into the DE-SG include an assessment of its inertia support capability. In [26], an adaptive control strategy is proposed to optimize this inertial response by accounting for damping currents during asynchronous operation.

The performance of the DE-SC in frequency regulation is clearly quantified in Table I.

TABLE I
COMPARISON OF FREQUENCY INDICES WITH AND WITHOUT THE DE-SC [26]

Application of DE-SC	f_{nadir}/Hz	$\mathrm{RoFoC}_{\max}/(\mathrm{Hz}\cdot\mathrm{s}^{-1})$
No	49.695	−0.52
Yes	49.876	−0.39

Furthermore, Fig. 10 illustrates the frequency response characteristics, highlighting the machine's ability to maintain grid frequency stability more effectively than conventional SCs during sudden load disturbances for two cases: Case 1—Frequency regulation is managed exclusively by the synchronous generator's governor, with a conventional condenser utilized in place of the DE-SC and Case 2—A coordinated approach is employed where both the synchronous generator's governor and the DE-SC contribute to frequency regulation [26].

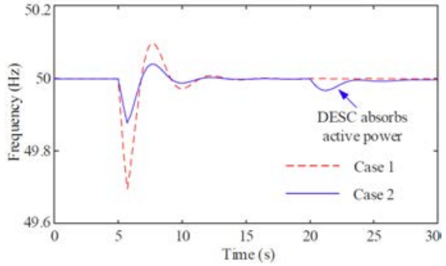

Fig. 10 Frequency fluctuations during load changes [26].

Another essential research direction in the performance analysis of dual-axis excited machines concerns the thermal limits imposed by reactive power consumption, as detailed in [27]. In this study, a 2D cross-section of the end region for both a traditional synchronous condenser (TSC) and a dual-axis excited synchronous condenser (DE-SC) is presented in Fig. 11, highlighting the structural complexity of the stator end components. The analysis reveals that while the DE-SC offers superior reactive power absorption capability by adjusting the magnetomotive force angle, this operating regime induces additional losses and temperature rises in the end zone. The article concludes that, unlike the TSC, where limits are more rigid, the DE-SC allows for more flexible operation; however, the maximum temperature recorded in the flux shields (pressure fingers) and in the end core packet becomes the critical factor restricting the maximum reactive power consumption capacity for both technologies [27].

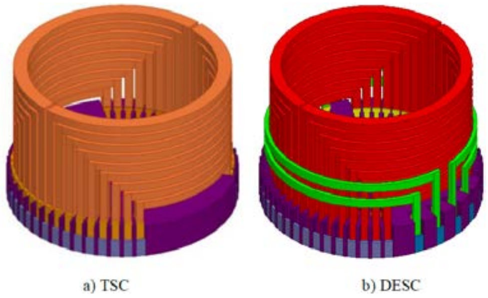

Fig. 11 2D-section of TSC and DE-SC [27].

In [28], the authors investigate the constructional features of the DE-SG, proposing two distinct field winding arrangements—one with an angular deflection and another with a 90° separation (d-q axis)—to effectively regulate frequency fluctuations in wind-integrated power grids. Their work, validated through ANSYS Maxwell (utilizing FEM) analysis, showed how these rotor configurations must be excited to ensure synchronous frequency at the stator terminals under variable speed. Complementing this structural analysis, [29] addresses the practical challenge of simulating such machines within standard software environments. Since platforms like MATLAB/Simulink lack a native DE-SG block, the study develops a comprehensive simulation model and provides direct verification of its accuracy. By comparing the custom model's response against established theoretical characteristics, this research provides a verified tool for further investigating the enhanced stability and independent control of the d-axis and q-axis excitation windings.

Another research has also focused on the fundamental electromagnetic relationships that govern the DE-SG operation. In [30], the authors investigate the relationship between excitation MMF under different operating modes, specifically comparing single-axis and dual-axis excitation. Using finite-element simulation, the study presents a unique rotor structure where slots are spaced equally over the entire surface, unlike traditional SGs. The most significant results from this research demonstrate that the DE-SG can maintain an air-gap flux density and EMF comparable to traditional machines while offering notably larger stability. A key result is the precise calculation of the MMF for various rotor slot pitches, proving that by independently adjusting the excitation currents in the two symmetrical field windings, the magnetic saturation in the stator and rotor cores can be effectively managed. These results, verified through both theoretical derivation and simulation, confirm that the DE-SG's structural flexibility allows it to enhance power supply reliability for critical users without compromising the core electromagnetic performance expected from standard synchronous technology [30].

To further advance the control capabilities of the DE-SG, research has moved toward nonlinear control strategies that account for real-world physical constraints. In [31], the authors propose a coordinated control scheme involving both dual-excitation and steam-valving by employing a bounded passivity-based design method. It is demonstrated in this paper that the proposed controller can achieve asymptotic stability for the closed-loop system even under arbitrarily bounded control inputs. This allows for an effective compromise between control performance and the energy magnitude of the control input, preventing the saturation of actuators. Simulation results verified that this passivity-based approach enables the DE-SG to converge to equilibrium states much more rapidly than traditional linear methods after a disturbance. By utilizing the port-controlled Hamiltonian system framework, this research provides a robust mathematical foundation for maintaining stability in DE-SG units subjected to varying operational limits [31].

The suitability of the DE-SG for wind energy applications is discussed in detail in [32].

The fundamental distinction between single and DE-SG lies in their operational flexibility and stability margins. While a single-excited generator relies on a single field winding on the d-axis, which ties its electromagnetic stability strictly to the excitation current and load angle, the DE-SG incorporates an additional excitation winding on the q-axis. This structural evolution leads to two advantages regarding control and response. Unlike single-excited machines, where increasing reactive power consumption often leads to instability near the static limit, the DE-SG allows for independent control of active and reactive power. By adjusting the MMF angle through dual-axis excitation, the machine can maintain a much wider stable operating region, even in deep under-excitation modes. Furthermore, from a grid-support perspective, single-excited units are limited by their synchronous speed for inertial response, whereas dual-axis excited machines can operate asynchronously for short periods via AC excitation, enabling them to release or absorb significantly higher amounts of kinetic energy. This makes the DE-SG a far more effective tool for frequency regulation and voltage stabilization in modern, low-inertia power systems, as shown in what follows.

IV. THE DE-SG FOR VARIABLE SPEED

Wind energy conversion, characterized by variable speed and power, is still dominated by the DFIG systems. The DE-SG may be considered a particular case of DFIG when:

1) The rotor has two symmetrical and distributed orthogonal (dq) windings fed from two single-phase inverters of fractional power ratings (Fig. 12(a)).

2) The control is modified for low variable rotor slip frequency as in DFIG (Fig. 12(b)).

The space phasor equations of this machine are [33]:

$$\begin{cases} \bar{\boldsymbol{v}}_{\mathrm{s}} = r_{\mathrm{s}} \cdot \bar{\boldsymbol{i}}_{\mathrm{s}} + l_{\mathrm{s}} \dfrac{\mathrm{d}\bar{\boldsymbol{i}}_{\mathrm{s}}}{\mathrm{d}t} + L_{\mathrm{m}} \dfrac{\mathrm{d}}{\mathrm{d}t}\left(\bar{\boldsymbol{i}}_{\mathrm{s}} + \bar{\boldsymbol{i}}_{\mathrm{f}} \mathrm{e}^{jp\theta_{\mathrm{r}}}\right) \\ \bar{\boldsymbol{v}}_{\mathrm{f}} = r_{\mathrm{f}} \cdot \bar{\boldsymbol{i}}_{\mathrm{f}} + l_{\mathrm{f}} \dfrac{\mathrm{d}\bar{\boldsymbol{i}}_{\mathrm{f}}}{\mathrm{d}t} + L_{\mathrm{m}} \dfrac{\mathrm{d}}{\mathrm{d}t}\left(\bar{\boldsymbol{i}}_{\mathrm{s}} \mathrm{e}^{-jp\theta_{\mathrm{r}}} + \bar{\boldsymbol{i}}_{\mathrm{f}}\right) \end{cases} \tag{11}$$

where L_{m} represents the mutual inductance of the synchronous machine, p represents the number of pole pairs, $\bar{\boldsymbol{v}}_{\mathrm{s}}$ and $\bar{\boldsymbol{v}}_{\mathrm{f}}$ represent the stator and excitation voltage space vector, and θ_{r} represents the angular position of the rotor frame with respect to the stator frame.

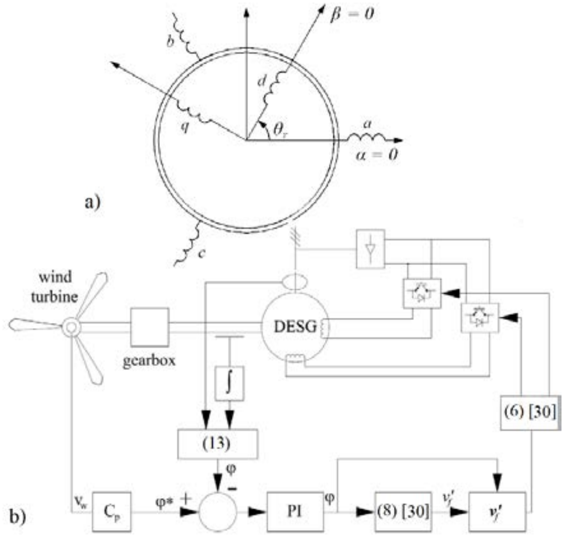

Fig. 12 (a) The windings. (b) The control of DE-SG for variable speeds [33].

(6) and (8) from Fig. 12(b) are from [33]. With:

$$\begin{cases} \bar{\boldsymbol{v}}_{\mathrm{s}} = v_{\mathrm{d}} + j \cdot v_{\mathrm{q}}; \quad \bar{\boldsymbol{v}}_{\mathrm{s}} = V_{\mathrm{s}} \cdot \mathrm{e}^{j\omega t} \\ \bar{\boldsymbol{i}}_{\mathrm{s}} = i_{\mathrm{d}} + j \cdot i_{\mathrm{q}}; \quad \bar{\boldsymbol{v}}_{\mathrm{f}} = v_{\mathrm{fd}} + j \cdot v_{\mathrm{fq}} \\ T_{\mathrm{el}} = \dfrac{3}{2} \cdot p \cdot L_{\mathrm{m}} \cdot \mathrm{imag}\left(\bar{i}_{\mathrm{s}} \cdot \bar{i}_{\mathrm{f}} \cdot e^{-jp\theta_{\mathrm{r}}}\right) \\ \dfrac{J}{p} \cdot \dfrac{\mathrm{d}\omega_{\mathrm{r}}}{\mathrm{d}t} = T_{\mathrm{el}} - T_{\mathrm{r}} \\ s(\mathrm{slip}) = \dfrac{\omega - \omega_{\mathrm{r}}}{\omega}; \quad \theta_{\mathrm{er}} = p \cdot \theta_{\mathrm{s}} \end{cases} \tag{12}$$

For steady state (d/dt = 0), with given load torque T_{r}, and with $V_{\mathrm{fd}} = V_{\mathrm{f}} \cdot \cos\varphi$ and $V_{\mathrm{fq}} = V_{\mathrm{f}} \cdot \sin\varphi$, a second order equation for $V_{\mathrm{f}} = V_{\mathrm{f}}^2 + B \cdot V_{\mathrm{f}} + C = 0$ for given φ is obtained [33] for each wind speed and power:

$$P_{\mathrm{t\,max}} = C_{\mathrm{p\,max}} \cdot \rho \cdot \pi \cdot R^2 \cdot v_{\mathrm{w}}^3 \tag{13}$$

where P_{tmax} represents the maximum turbine power, C_{pmax} represents the maximum power coefficient, ρ is the air density, and v_{w} represents the wind speed.

Consequently, the efficiency is:

$$\eta = \frac{P_{\mathrm{s}} + P_{\mathrm{t}}}{P_{t\,\mathrm{max}}} = \frac{3 \cdot \mathrm{Re}\left(\bar{\boldsymbol{v}}_{\mathrm{s}} \cdot \bar{\boldsymbol{i}}_{\mathrm{s}}^{*} + \bar{\boldsymbol{v}}_{\mathrm{f}} \cdot \bar{\boldsymbol{i}}_{\mathrm{f}}^{*}\right)}{P_{t\,\mathrm{max}}} \tag{14}$$

So, efficiency for $\left|\bar{\boldsymbol{V}}_{\mathrm{f}}\right| = V_{\mathrm{f}}$ and $V_{\mathrm{f}}^2 + B \cdot V_{\mathrm{f}} + C = 0$ depends on the angle φ which represents the phase angle between the stator voltage vector and the excitation (rotor) voltage vector $\bar{\boldsymbol{V}}_{\mathrm{s}}$ and $\bar{\boldsymbol{V}}_{\mathrm{f}}$. A maximum efficiency table for φ_{optim} (v_{w}) or for ω_{r} is obtained, and may be used as feedback for $\varphi_{\mathrm{control}}$ (Fig. 12(b)).

But angle φ in the steady state is:

$$\varphi = p \cdot \theta_{\mathrm{r}} + \psi - \omega t \tag{15}$$

Here, $\psi = \tan^{-1}(V_{\mathrm{fq}}/V_{\mathrm{fd}})$ and θ_{r} denotes the rotor d-axis angle relative to stator phase a.

For a 2.5 MW wind generator with:

V_{sn} = 6 kV, R_{s} = 0.3 Ω, R_{f} = 0.15 Ω, L_{m} = 0.17 H, L_{f} = 6.4 mH, p = 2, J = 430 kg·m², Fig. 13 [33] shows the step speed response of a DE-SG vs. cage induction generator (IG), during starting at a wind speed, $v_w = 9$ m/s while at $t = 12$ s a step charge of wind speed of +3 m/s is simulated. For the IG, the speed changes a little (from 1508 to 1517 r/min) while for the DE-SG with the control for maximum efficiency, the speed changes from 1495 to 1618 r/min (for $C_{pmax} = 0.47$) (Fig. 13). It should be noted that the stator currents in DE-SG are smaller, and a +2% efficiency and +40 kW power are obtained, while the dq excitation currents are symmetric and increase their "slip frequency" (Fig. 13(c))), when the wind speed changes. In a subsequent paper [34], the authors of [33] have developed a particular active control of power to the rotor windings down to zero in supersynchronous operation.

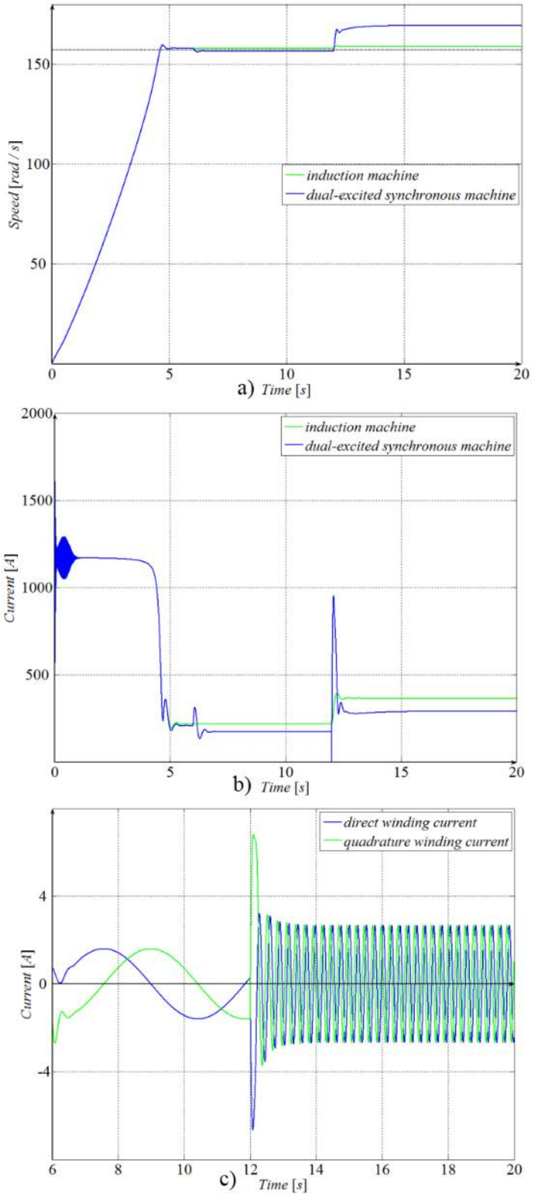

Fig. 13 (a) Speed response of a DE-SG vs. IG for step wind speed at max efficiency. (b) Amplitude of stator currents. (c) dq-axis excitation currents during the transients [33].

In this case, the grid side inverter in the back-to-back converter that feeds the rotor windings could be a diode rectifier, which means lower costs Fig. 14.

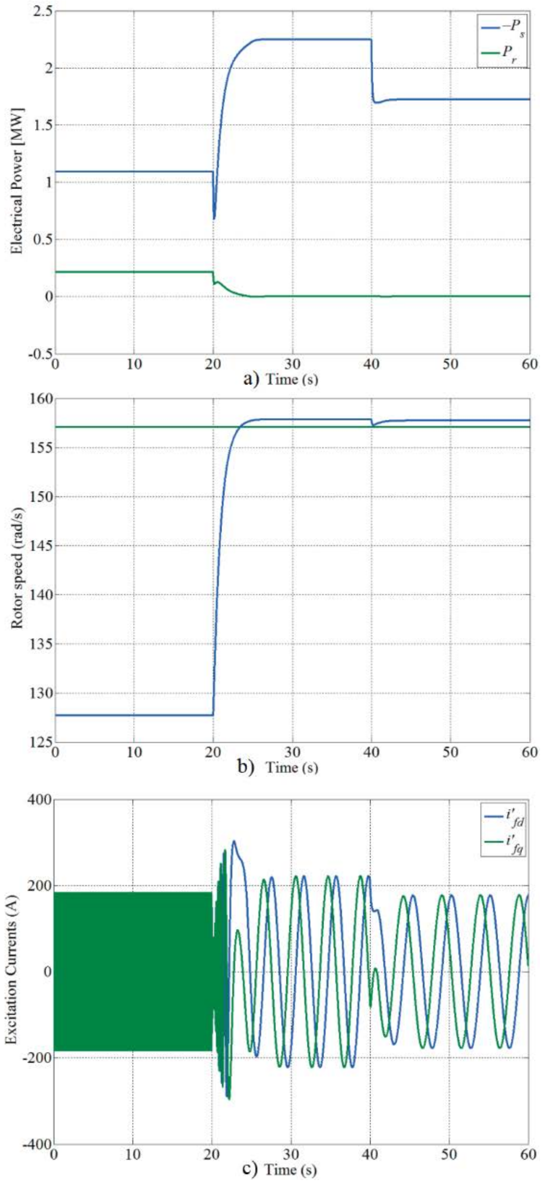

Fig. 14 2.5 MW DE-SG case study. (a) Stator and rotor active power. (b) Rotor speed and synchronous speed. (c) Rotor dq-axis currents [34].

At lower than standard synchronous speed, the rotor power is absorbed ($P_r > 0$), and at supersynchronous speed, P_r is controlled to be zero to meet the diode rectifier requirements. Also, the stator power factor was improved to almost unity in Fig. 14 [34].

As expected, the slip frequency of rotor dq-axis currents is reduced in the supersynchronous operation at $P_r = 0$. Some recent control of DE-SG concentrates on constant speed, constant frequency, but variable absorbed reactive power [32].

V. THE DE-SC

As mentioned earlier, there is frequently an excess of voltage due to, say, PV power sources in modern power systems. In an SE-SC, it means to reduce the d-axis field current close to zero. But this means that the SC (in fact a synchronous machine in no-load motoring conditions) becomes unstable as the power angle δ (between $\overline{\boldsymbol{V}}_s$ and $\overline{\boldsymbol{E}}_q$)

will be too large. In an DE-SC, with $\alpha = \arctan(E_{\text{fd}}/E_{\text{fq}})$ (Fig. 15(b) [19]), the angle δ of $\bar{\boldsymbol{E}}_{\text{f}}$ with respect to $\bar{\boldsymbol{V}}_{\text{f}}$ is reduced considerably. Here, α is the angle that the EMF phasor leads q axis and E_{fd}, E_{fq} represent the dq-axis components of the excitation voltage.

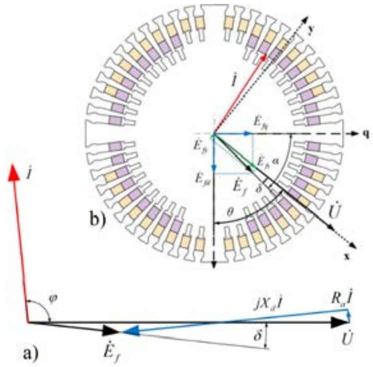

Fig. 15 (a) DE-SC phasor diagram. (b) Symmetrical dual excitation scheme with phasor diagram [19].

The active and reactive powers in an SE-SC are (Fig. 9(a) [19]):

$$\begin{cases} P = E \cdot V_{\text{s}} \cdot \sin\delta; \\ Q = \dfrac{E \cdot V_{\text{s}}}{X_{\text{s}}} \cdot \cos\delta - \dfrac{V_{\text{s}}^2}{X_{\text{s}}} \end{cases} \tag{16}$$

This time:

$$\delta = \alpha + \theta + \pi/2 \tag{17}$$

and the active and reactive power of DE-SC are [19]:

$$\begin{cases} P = 3 \cdot \dfrac{V_{\text{s}} \cdot E_{\text{f}}}{X_{\text{d}}} \cdot \sin\delta = 3 \cdot \dfrac{V_{\text{s}} \cdot E_{\text{s}}}{X_{\text{d}}} \cdot \cos(\alpha + \theta) \\ Q = 3 \cdot \left(-\dfrac{X_{\text{s}}^2}{X_{\text{d}}} - \dfrac{V_{\text{s}} \cdot E_{\text{f}}}{X_{\text{d}}} \cdot \sin(\alpha + \theta) \right) \end{cases} \tag{18}$$

Alternatively,

$$\begin{cases} P = 3 \cdot \dfrac{V_{\text{s}}}{X_{\text{d}}} \cdot \left(E_{\text{q}} \cdot \sin\delta + E_{\text{d}} \cdot \cos\delta \right) \\ Q = 3 \cdot \left(\dfrac{E_{\text{q}} \cdot V_{\text{s}}}{X_{\text{s}}} \cdot \cos\delta - \dfrac{E_{\text{d}}}{X_{\text{s}}} \cdot \sin\delta - \dfrac{V_{\text{s}}^2}{X_{\text{s}}} \right) \end{cases} \tag{19}$$

It becomes more evident now that the reactive power Q, may be controlled by E_{q} (via i_{fd}, even negative) while the active power P may be controlled by E_{d} (via i_{fq}). Voltage for Q power and speed for P active power tracking may thus be conceived as in Fig. 16 [8].

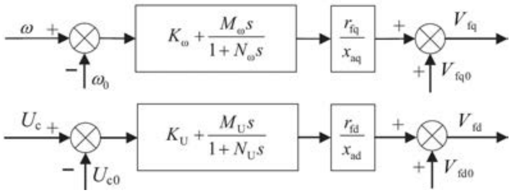

Fig. 16 Block diagram of voltage and speed control of DE-SC [8].

Sample dynamic simulation results of such a control system for a 10 kW lab DE-SC prototype [2] shows stable response in voltage when large negative i_{fd} is notable, under sudden increase of power system voltage Fig. 17.

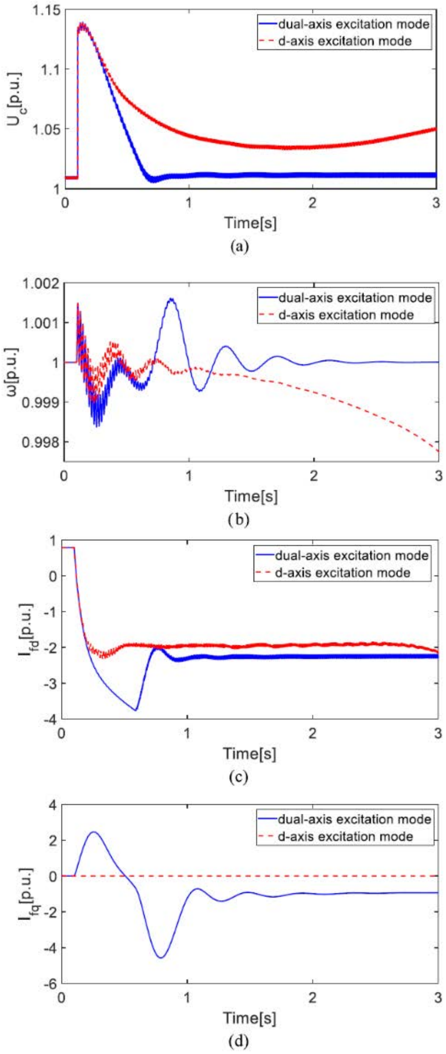

Fig. 17 DE-SC response to sudden change of system terminal voltage U_{c} (p.u.). (a) Terminal voltage. (b) Rotor speed. (c) d-axis excitation current i_{fd}. (d) q-axis excitation current i_{fq} [8].

As visible in Table II, the reactive power consumption is enhanced spectacularly with DE-SC, up to −2.69 p.u. for a $\Delta V = 20\%$ (voltage swell). In some contrast, non-conductive wedges in the rotor slots lead to spectacularly smaller i_{fdmax} (negative) in comparison to copper wedges for about the same transient reactive power $Q_{\text{T}} \approx -1.5$ p.u. of the machine. The dq-axis symmetric distributed windings are considered superior to asymmetric windings [8]. Asymmetric in the sense that their MMFs would be different for the dq-axis excitation windings.

TABLE II
REACTIVE POWER CONSUMPTION OF DE-SC VS. $\Delta V > 0$ [8]

	ΔV/%	5	10	20	30	36	37
TSC	Q_{T}/p.u.	0.62	–0.7				
	Recovery of U_{c}	Yes			No		
DE-SC	Q_{T}/p.u.	1.49	1.49	2.69	3.81	4.38	4.40
	Recovery of U_{c}			Yes			No

Discussions on DE-SC recent progress

It should be obvious from the case stability illustrated in Fig. 17 and Table II that the DE-SC is capable to produce much more absorbed reactive power (by negative i_{df}) and remain stable (by i_{qf} intervention). However, as shown in the same figure (Fig. 17), caution is necessary since the required excitation currents reach high p.u. values; consequently, a robust design must account for these thermal and operational constraints.

Due to space limitations, we examine here a few recent developments in SCs.

For instance, [35] investigates the application of SCs alongside grid-type static VAR generators (SVGs), revealing that while both provide reactive power support, the SC offers distinct advantages in dynamic regulation and harmonic suppression when evaluated through dual closed-loop and virtual synchronous generator (VSG) control strategies. From an infrastructural standpoint, [36] highlights the economic viability of converting decommissioned thermal power units into SCs, demonstrating through both digital and physical simulations that such conversions significantly enhance transient voltage stability within substation environments. Furthermore, since the operational efficacy of these machines relies heavily on precise characterization, [37] proposes a sophisticated parameter identification method for novel SCs; this approach utilizes DC step voltage tests combined with particle swarm optimization and wavelet transforms to refine the accuracy of 2D finite element analysis (FEA) models.

Regarding the integration of large-scale SCs, an improved phase angle prediction method for quasi-synchronous grid connection is proposed in [38]. To ensure a safe and stable synchronization, the study establishes a rigorous set of rules for grid synchronization: the maximum allowable deviations for amplitude ($\leq 1\%$), frequency (≤ 0.25 Hz), and phase angle ($\leq 2^{\circ}$) during the closing process.

Beyond providing voltage and reactive power support, SCs integrated with flywheels represent a key solution for enhancing system inertia. However, as investigated in [39], the mechanical coupling of a flywheel introduces complex torsional modes that can interact with the electrical grid. To analyze these phenomena, the authors employ a two-mass drive train model to represent the flywheel and rotor system, as illustrated in Fig. 18 (with the results given in Fig. 19) which serves as the basis for studying torque amplification and potential unstable oscillations, considering that: τ_f, θ_f, ω_f and τ_r, θ_r, ω_r represent the input torque, angular displacement, and angular velocity of the flywheel and the rotor, respectively. H_f and H_r represent the flywheel and the rotor moment of inertia; K_s and D_s represent the torsional stiffness and damping coefficient.

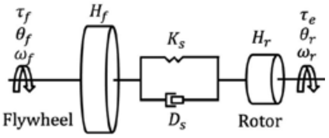

Fig. 18 Two-mass drive train model for flywheel and rotor system simulation [39].

The impact of these torsional dynamics is quantified through the Bode plot of self-impedance and transfer impedance (Fig. 19), which highlights how different mechanical modes (e.g., 10 and 20 Hz) and damping ratios (ζ_m) influence the system's impedance profile.

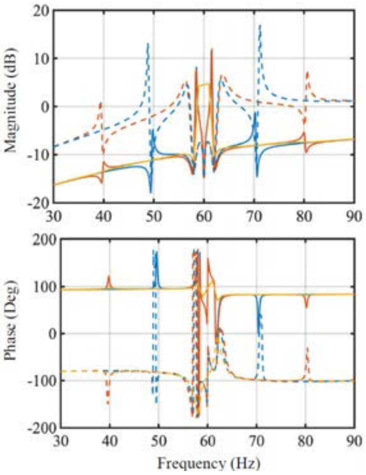

Fig. 19 Bode plot: self-impedance with solid line, and transfer impedance with dashed line of 10 Hz mechanical mode (blue lines), 20 Hz mechanical mode with $\zeta_d = 0.001$ with orange lines, and 20 Hz mechanical mode with $\zeta_d = 0.1$ with gold lines [39].

Another role of SCs is in reinforcing power grids with high renewable energy penetration, where voltage stability is often compromised. In [40], the authors develop a configuration strategy that utilizes SCs to solve overvoltage issues by analyzing their impact on the multiple renewable energy stations short circuit ratio (MRSCR). Ultimately, this approach optimizes the deployment process, ensuring system stability while effectively reducing the required number of SC units. The structural integration of these units within the network is represented in Fig. 20, which illustrates a simplified schematic of multiple renewable energy stations connected to the grid.

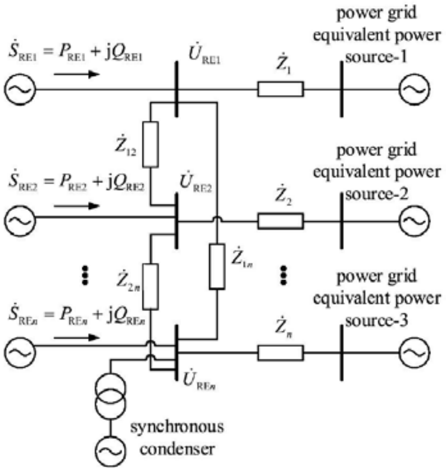

Fig. 20 Multiple renewable energy stations connected with the AC grid with an SC [40].

S_{RE}, P_{RE}, Q_{RE}, and U_{RE} represent the renewable energy source's apparent, active, reactive powers, and voltage, and Z represents the impedance of the AC grid integration bus.

Furthermore, the operational effectiveness of the SC in modern power systems relies heavily on the accuracy of its mathematical model and parameters. In [41], the authors address the challenges of parameter identification by employing a sensitivity analysis to determine which internal parameters most significantly impact the device's performance. By focusing on the most influential variables, the study proposes an optimized identification method that enhances the precision of the SC model, ensuring its control systems can accurately respond to dynamic grid fluctuations and provide reliable reactive power support.

Beyond modeling and configuration, maintaining the operational reliability of the SC is essential, leading to the development of advanced monitoring techniques. In [42], a specialized fault diagnosis method for the SC is introduced, utilizing a radial basis function (RBF) neural network. This approach focuses on identifying internal mechanical and electrical faults by processing vibration signals and operational data, allowing for early detection of abnormalities. By implementing this intelligent diagnostic framework, the system can ensure the long-term availability of the SC, preventing unexpected outages and securing its role as a dependable source of inertia and voltage support for the grid.

While previous studies focus on general placement and fault detection, recent research has shifted toward the refined internal control dynamics necessary for the SC to stabilize wind-integrated weak grids. Unlike traditional installations that use fixed or standard control settings, the study in [43] introduces a state-space based analysis to investigate how inter-parametric variations—such as exciter gain, transient reactance, and inertia—directly influence oscillation damping and grid resilience. The authors propose a "parametrically optimized coordinated control" framework that outperforms conventional "one-size-fits-all" configurations by adapting the device's response to the specific impedance characteristics of a weak grid. Specifically, Fig. 21 [43], demonstrates the superior voltage recovery performance under a fault scenario in a weak grid, showing that the proposed control strategy allows the SC to restore terminal voltage more rapidly and with fewer oscillations compared to standard existing control models. Another interesting investigation is presented in [44], where the simulation results are shown in Fig. 22 based on the machine parameters provided in Table III.

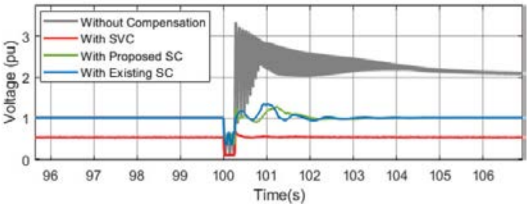

Fig. 21 Point of common coupling voltage during fault in a weak grid with SVC, with proposed and existing SC [43].

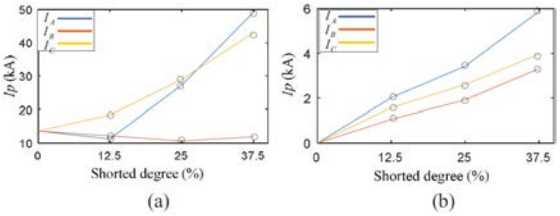

(a) (b)

Fig. 22 (a) First current harmonic under different levels of fault degree. (b) Third current harmonic under different levels of fault degree [44].

TABLE III
300 MVAR SC SIMULATION
PARAMETERS [44]

Parameter	Value	Parameter	Value
Pole pairs	1	Stator outside diameter/mm	2500
Rated capacity/MVAR	300	Stator inner diameter/mm	1240
Maximum reactive power absorption/MVAR	211	Rotor outside diameter/mm	1100
Rated power factor	0	Air gap/mm	70
Rated voltage/kV	20	Stator slots	48
Rated stator current/A	8660	Rotor slots	32
Rated exciting voltage/V	415	Rated speed/(rot·min^{-1})	3000
Rated exciting current/A	1835	No-load exciting voltage/V	143V
Rated frequency/Hz	50	No-load exciting current/A	735A

In this study, the authors employ third-harmonic currents as a diagnostic indicator for stator inter-turn short-circuit faults in the SC. The authors claim that the third harmonic of the three-phase current increases progressively with the severity of the fault. This observed generation of the third harmonic is consistent with respect to the increase of the fault severity (Fig. 22).

Within the context of a grid increasingly dominated by PV generation, the authors of [45] evaluate several strategies for enhancing system strength. Specifically, they analyze the control of the SCR using SCs in comparison to SVCs and STATCOMs.

The practical feasibility of integrating SCs into modern power electronics-based grids is extensively documented in literature. Specifically, in [46], the authors provide unique insights into the performance of a real MW-scale islanded system, which integrates a 2.2-MVA grid-forming (GFM) and grid-following (GFL) battery energy storage system alongside 2.5-MVA SCs and a 3-MVA load bank.

By mimicking the challenges typical of larger power systems, [46] demonstrates both stable operation in Fig. 23 across various resource combinations and seamless mode transitions, including the critical scenario involving the loss of the last SG.

Regarding the experimental results, the authors present several fault scenarios, including a case study on the islanding transition of the GFM inverter, the SC, and the load. As illustrated in Fig. 23, the island is formed at t = 0.9 s; at this moment, the GFM-based battery energy storage systems (BESSs) successfully assume the 500-kW load, while the SC provides the necessary reactive power support to maintain system stability.

VI. THE DFIG AS A MFG SYSTEM WITH RECONFIGURABLE CONTROL (PROPOSED)

As known, two orthogonal and symmetric distributed windings in the rotor (BE-SG or BE-SC) are equivalent with three symmetric (120º shifted) windings (as in DFIG). This is how, by a few changes, the DFIG may become MFG, via a few additional power switches (Fig. 24) and by reconfigurable control.

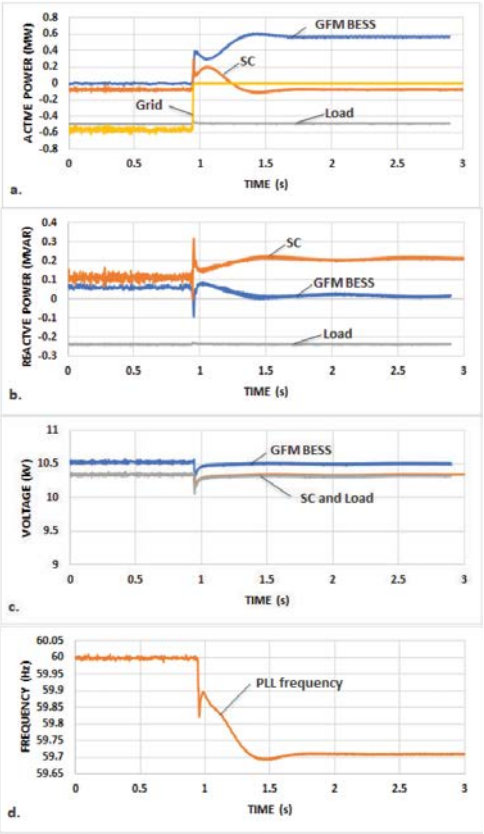

Fig. 23 GFM inverter with 5% drop, SC and load: grid connection loss at t = 0.95 s [46].

The hardware additions of the here proposed modified DFIG (Fig. 24) may be achieved as:

1) Adding a rotor-null connected slip ring and brush to make a 4-leg MSC (machine-side AC-DC converter).

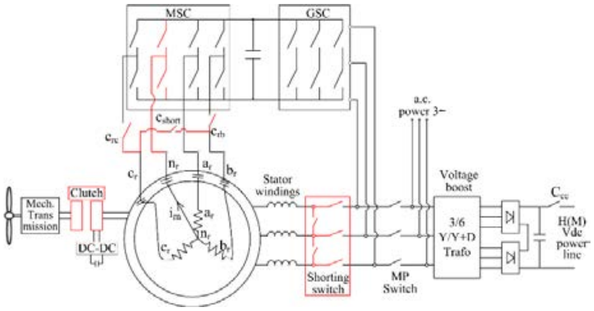

Fig. 24 The proposed MFG DFIG scheme.

2) Adding a 3-pole power switch in front of MSC that disconnects phases b and c in the rotor from the MSC, but short circuits them by an electromechanical (or a thyristor) device, to make a q-axis cage in the rotor; while the null n and the phase a connections provide DC controlled d-axis excitation of DFIG working as in SG or SC-when the clutch is opened to allow no load motoring.

3) Adding a stator power separation by a shorting stator switch (shorting stator switch) to extract more wind power at lower speed by operating it as IG fed via grid side converter (GSC) connected to the *ac* power grid (where available);

4) Adding a 3/6 phase (Y||Y+D) voltage boost transformer plus a 6-phase diode rectifier to provide controlled M(H) DC voltage output for making the sending of a M(H) VDC power transmission line option, as DFIG or as a DC excited SG.

5) Adding a PM electrically controlled induction clutch (where it does not exist) to disengage the idle turbine and thus allow dual-axis excited SC mode for more reactive power control.

Summarizing, the multiple operating modes are (Fig. 24):

1) Standalone DFIG: with the rotor neutral current: $i_{rn} = 0$;

2) Synchronous generator with q-axis cage $i_m \neq 0$, $i_{ardc} = i_{exc}$, $i_{b_r} = -i_{c_r}$ (b_r and c_r phases are shorted together).

3) Single-excited SC: as case 2 but with open clutch for idle turbine separation.

4) Dual-axis excited SC with phase a_r and n_r as d-axis excitation and b_r and c_r phases in counter series as q-axis excitation.

5) Dual-axis excited SG as in case 4 but with the clutch closed, to absorb more reactive power and provide more stability.

6) Shorted stator rotor -fed IG for more output power at low speeds (through MSC + GSC + AC grid)

7) Fractional reactive power delivery (form DC-link capacitor with GSC at an AC power grid) with the turbine at standstill (clutch open).

8) Operation only with the 12-pulse diode rectifier output when the SE or DE-SG will regulate output DC voltage at constant or variable speeds, by the MSC control.

9) Controlling the DFIG with diode rectified output allowing variable stator frequency for better efficiency and high speeds.

10) Controlling the ac grid connected DE-SG asynchronous (with slip frequency in the dual-axis excited rotor) with zero active power from the rotor when the GSC is working only as a diode rectifier. The control of constant dc output voltage at variable speed is done through MSC.

Note 1: When the standalone DFIG is used with dual excitation, and additional brush, to provide symmetric rotor MMFs, the current in phase a will be $\sqrt{3}$ times higher than in phase b–c unless, from start, the DFIG is made with symmetric orthogonal excitation windings.

Note 2: MFG physical concept with reconfigurable control was conceived to operate as an SG or SC with a single excitation or with dual excitation both at constant and variable speed.

Note 3: A DFIG may be used as basis, since as the three phase AC rotor winding may work as a d–q excitation in AC with vector control, with max. slip values up to ±30% (in general) as usual. In this case, no additional brush is required but the possibility to build a strong cage winding in axis q, for synchronous (zero slip) operation is lost.

VII. DFIG WITH DIODE RECTIFIER CONTROLLED OUTPUT (A CASE STUDY FOR MFG GENERATOR)

In order to exemplify the DFIG as a MFGl generator designed to reduce costs in a decentralized controlled H(M) VDC interface for power transmission lines, the schematic in

Fig. 25 is presented. This configuration, analyzed in [47], utilizes a specialized transformer with star and delta connections on the secondary side linked to a 12-pulse rectifier, optimizing the interface for standalone applications. As illustrated by the control block diagram in Fig. 26, typical simulation results are shown in Fig. 27, where the DFIG system currents and voltages are presented during system loading.

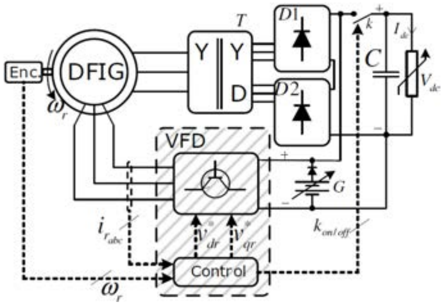

Fig. 25 Control schematic diagram for simulation [47].

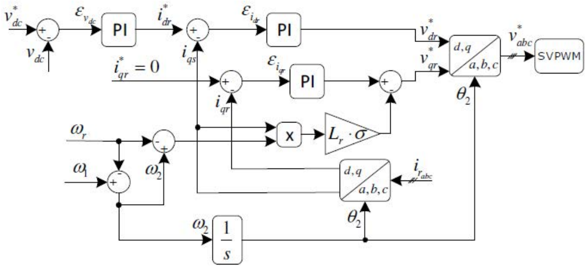

Fig. 26 DFIG rotor-side converter control diagram [47]

Furthermore, the study in [47] highlights that the implementation of a rotor current-oriented control strategy effectively minimizes cross-coupling effects, ensuring robust dynamic performance during start-up and under varying load conditions, as evidenced by the DC-link voltage (V_{dc}) stability maintained throughout the simulations (Fig. 27).

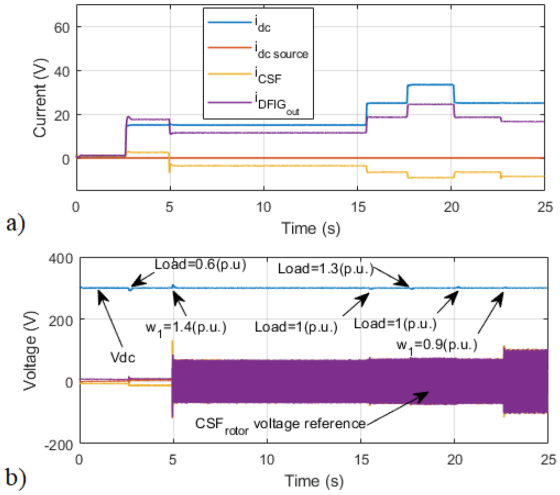

Fig. 27 System currents. (a) DC current produced by the low-voltage source, the rotor converter's absorbed current, and DFIG DC output current. (b) DC voltage and rotor converter's reference voltages during DFIG system loading [47].

Moreover, it is demonstrated in Fig. 28 that allowing the stator frequency to vary with speed (in addition to the lower, variable frequency in the rotor), the overall efficiency of the generator can be increased by 1%–3%.

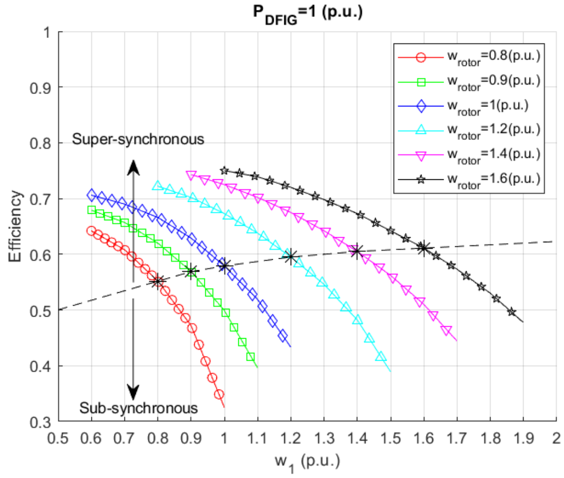

Fig. 28 System efficiency for 1 p.u. DFIG power, for different wind speeds and different stator frequencies [47].

VIII. CONCLUSION

Decades ago it was demonstrated that the DE-SG stability zone and its reactive power consumption can be enhanced in comparison with the traditional single-excited SG (SE-SG) [8]. Recently the DE-SG principle has been extended to variable speed SGs and to DE-SC with the main purpose to assist frequency and voltage stabilization in modern energy systems with ever larger penetration of renewable energy sources.

To demonstrate the high level of interest in dual excitation, a very recent study [48] proposes a configuration where a traditional synchronous generator is mechanically coupled with a dual-excitation synchronous machine. Connected in series along the transmission line, this system aims to enhance the power transfer capacity to the point of common coupling (PCC) in modern power systems.

The review paper here, treated a few key issues with DE-SG and DE-SC to the point of proposing a DFIG with 10 operation modes via a few additional power switches and by reconfigurable control.

It is hoped that the humble effort here will inspire new interesting work for extending the use of DE-SG [32] and DE-SC for constant and variable speed operation for frequency and voltage stabilization; especially through a better use of mechanical inertia of such systems [49], which is not easy to produce with power electronics systems (STATCOMs, etc.).

REFERENCES

[1] S. Kalsi, D. Madura, and M. Ross, "Performance of Superconductor Dynamic Synchronous Condenser on an Electric Grid," in *Proc. of 2005 IEEE/PES Transmission & Distribution Conference & Exposition: Asia and Pacific*, Dalian, China, Aug. 2005, pp. 1–5.

[2] P. Hsu, E. Muljadi, and Z. P. Wu *et al.*, "Voltage Regulation Using a Permanent Magnet Synchronous Condenser with a Series Compensator," in *Proc. of 2015 IEEE Energy Conversion Congress and Exposition (ECCE)*, Montreal, QC, Canada, Sept. 2015, pp. 5851–5856.

[3] P. Hsu, and E. Muljadi, "Permanent Magnet Synchronous Condenser for Wind Power Plant Grid Connection Support," in *Proc. of 2015 9th*

International Conference on Power Electronics and ECCE Asia (ICPE-ECCE Asia), Seoul, Korea (South), Jun. 2015, pp. 362–366.

[4] W. M. Tong, P. Wang, and S. N. Wu *et al*., "Electromagnetic Performance Analysis of a Hybrid Excitation Synchronous Machine based on 3D Equivalent Magnetic Network," *Transactions of China Electrotechnical Society*, vol. 38, no. 3, pp. 692–702, Feb. 2023.

[5] X. T. Xiao, L. L. Hao, and Z. Q. Liang *et al*., "Analysis of Generator Loss of Field Fault in Nuclear Power Plant Control Rod Power System," *Transactions of China Electrotechnical Society*, vol. 38, no. 3, pp. 770–780, Feb. 2023.

[6] M. Singh, M. A. Ansari, and N. S. Pal *et al*., "Comparison of Control Techniques for Damping of Oscillations in Power System Using STATCOM," in *Proc. of 2018 International Conference on Computational and Characterization Techniques in Engineering & Sciences (CCTES)*, Lucknow, India, Sept. 2018, pp. 188–191.

[7] S. U. Mahmud, and N. A. Masood, "Performance Comparison between Synchronous Condenser and Static VAR Compensator to Improve System Strength in a Wind Dominated Power Grid," in *Proc. of 2020 11th International Conference on Electrical and Computer Engineering*, Dhaka, Bangladesh, Dec. 2020, pp. 411–414.

[8] G. R. Xu, L. G. Wang, and Z. J. Li *et al*., "Improvement of Reactive Power Consumption Ability for Dual-excited Synchronous Condenser," *IEEE Transactions on Industry Applications*, vol. 60, no. 4, pp. 6056–6065, Jul.-Aug. 2024.

[9] G. R. Xu, Z. J. Li, and Z. Z. Wang *et al*., "Power Tracking Excitation Control and Its Parameter Optimization of Dual-excited Synchronous Generator," *IEEE Trans. on Ind. Applicat*., vol. 58, no. 6, pp. 7099–7109, Nov.-Dec. 2022.

[10] Y. Y. Zhao, J. Y. Chai, and X. D. Sun, "Virtual Synchronous Control of Grid-connected DFIG-based Wind Turbines," in *Proc. of 2015 IEEE Applied Power Electronics Conference and Exposition (APEC)*, Charlotte, NC, USA, Mar. 2015, pp. 2980–2983.

[11] Z. L. Li, and F. Liu, "Frequency and Voltage Regulation Control Strategy of Wind Turbine based on Supercapacitors Under Power Grid Fault," *Energy Reports*, vol. 10, pp. 2612–2622, Nov. 2023.

[12] H. Nian, and Y. Z. Jiao, "Improved Virtual Synchronous Generator Control of DFIG to Ride-through Symmetrical Voltage Fault," *IEEE Transactions on Energy Conversion*, vol. 35, no. 2, pp. 672–683, Jun. 2020.

[13] F. Z. Zahid, M. Wali, and G. E. M. Abro, "Voltage and Frequency Control of A Synchronous Generator Implementing Fuzzy Logic Approach," in *Proc. of 2024 1st International Conference on Innovative Engineering Sciences and Technological Research (ICIESTR)*, Muscat, Oman, May 2024, pp. 1–6.

[14] W. J. Chen, F. Blaabjerg, and N. Zhu *et al*., "Doubly Fed Induction Generator Wind Turbine Systems Subject to Recurring Symmetrical Grid Faults," *IEEE Transactions on Power Electronics*, vol. 31, no. 2, pp. 1143–1160, Feb. 2016.

[15] C. Li, Y. Q. Yang, and Y. J. Cao *et al*., "Frequency and Voltage Stability Analysis of Grid-forming Virtual Synchronous Generator Attached to Weak Grid," *IEEE Journal of Emerging and Selected Topics in Power Electronics*, vol. 10, no. 3, pp. 2662–2671, Jun. 2022.

[16] X. L. Xiong, C. Wu, and F. Blaabjerg, "An Improved Synchronization Stability Method of Virtual Synchronous Generators based on Frequency Feedforward on Reactive Power Control Loop," *IEEE Transactions on Power Electronics*, vol. 36, no. 8, pp. 9136–9148, Aug. 2021.

[17] A. Safaeinejad, M. Rahimi, and D. Zhou *et al*., "Wind Turbulence-induced Power Fluctuations Mitigation in PMSG-based Wind Turbines by a Coordinated Control Scheme," *IEEE Transactions on Sustainable Energy*, vol. 17, no. 1, pp. 58–69, Jan. 2026.

[18] "Synchronous Condenser (SynCon) for Grid Stability and Efficiency," Accessed: Feb. 2, 2026. [Online]. Available: https://www.siemens-energy.com/global/en/home/products-services/product/synchronous-condenser.html

[19] F. Q. Zhou, X. T. Wang, and Z. Y. Zhao *et al.*, "Reactive Power Absorption Capability of Dual-excited Condenser with Symmetric Excitation Scheme," in *Proc. of 2024 The 9th International Conference on Power and Renewable Energy (ICPRE)*, Guangzhou, China, Sept. 2024, pp. 530–534.

[20] S. C. Kapoor, S. S. Kalsi, and B. Adkins, "Improvement of Alternator Stability by Controlled Quadrature Excitation," *Proceedings of the Institution of Electrical Engineers*, vol. 116, no. 5, pp. 771–780, May 1969.

[21] H. C. Agarwal, and S. C. Kapoor, "Power System Dynamic Studies for Improved Stability and Minimum Rotor Heating via Graph-theoretic Modelling of a Dual-excited Synchronous Generator," *IEEE Transactions on Power Apparatus and Systems*, vol. 94, no. 2, pp. 177–186, Mar. 1975.

[22] A. M. El-serafi, and M. A. Badr, "Analysis of the Dual-excited Synchronous Machine," *IEEE Transactions on Power Apparatus and Systems*, vol. PAS-92, no. 1, pp. 1–8, Jan. 1973.

[23] A. M. El-serafi, and M. A. Badr, "Extension of the Under-excited Stable Region of the Dual-excited Synchronous Machine," *IEEE Transactions on Power Apparatus and Systems*, vol. PAS-92, no. 1, pp. 287–294, Jan. 1973.

[24] G. R. Xu, B. Y. Li, and Y. Zhan *et al*., "Numerical Calculation of Transient Parameters of Dual-excited Synchronous Generator based on Time-stepping Finite Element Model," in *Proc. of 2023 IEEE Energy Conversion Congress and Exposition (ECCE)*, Nashville, TN, USA, Oct. 2023, pp. 4954–4958.

[25] G. R. Xu, Y. Fu, and Z. Z. Wang *et al*., "Influence of Rotor Damping Effect on Dynamic Characteristic of Dual-excited Synchronous Generator with Excitation Control," in *Proc. of 2022 IEEE Energy Conversion Congress and Exposition (ECCE)*, Detroit, MI, USA, Oct. 2022, pp. 1–6.

[26] G. R. Xu, G. L. Yang, and Z. C. Cao *et al*., "Inertial Support Capability of Dual-excited Synchronous Condenser Using Adaptive Control Strategy in Renewable Energy Systems," in *Proc. of 2025 IEEE Energy Conversion Conference Congress and Exposition (ECCE)*, Philadelphia, PA, USA, Oct. 2025, pp. 1–6.

[27] G. R. Xu, X. Jin, and Z. Q. Li *et al*., "Influence of Temperature Rise in Stator End Region on Reactive Power Consumption Ability of Dual-excited Synchronous Condenser," *IEEE Transactions on Industry Applications*, vol. 60, no. 6, pp. 8585–8595, Nov.-Dec. 2024.

[28] A. A. Reddy, and S. S. Bhat, "Modeling of Dual Excited Synchronous Generator with Slip Frequency Excitation," in *Proc. of 2020 IEEE First International Conference on Smart Technologies for Power, Energy and Control (STPEC)*, Nagpur, India, Sept. 2020, pp. 1–3.

[29] L. H. Chen, Q. P. Xu, and Y. T. Shi *et al*., "Simulation Modeling and Simulation Verification of Dual-excited Synchronous Generator," in *Proc. of 2024 IEEE 4th New Energy and Energy Storage System Control Summit Forum (NEESSC)*, Hohhot, China, Aug. 2024, pp. 98–104.

[30] G. R. Xu, Y. P. Hu, and X. J. Hao *et al.*, "The Relationship of Magnetomotive Force Under Different Excitation Modes of Dual-excited Synchronous Generator," *IEEE Transactions on Magnetics*, vol. 54, no. 3, pp. 1–4, Mar. 2018.

[31] B. Wang, and W. Lin, "Bounded Control of Dual-excited Synchronous Generator by Using a Passivity-based Approach," in *Proc. of 2011 9th World Congress on Intelligent Control and Automation*, Taipei, Taiwan, Jun. 2011, pp. 85–90.

[32] R. R. Abdel-Wahab, H. M. Yassin, and H. H. Hanafy, "Dual Excited Synchronous Generator a Suitable Alternative for Wind Applications," in *Proc. of 2020 IEEE 14th International Conference on Compatibility, Power Electronics and Power Engineering (CPE-POWERENG)*, Setubal, Portugal, Jul. 2020, pp. 352–357.

[33] L. Piegari, R. Rizzo, and P. Tricoli, "High Efficiency Wind Generators with Variable Speed Dual-excited Synchronous Machines," in *Proc. of 2007 International Conference on Clean Electrical Power*, Capri, Italy, May 2007, pp. 795–800.

[34] S. D'Arco, L. Piegari, and P. Tricoli, "A Novel Control of Dual-excited Synchronous Machines for Variable-speed Wind Turbines," in *Proc. of 2011 IEEE Trondheim PowerTech*, Trondheim, Norway, Jun. 2011, pp. 1–6.

[35] Z. Y. Zhao, Q. Liu, and N. H. Chen, "Comparative Study on Control and Stability of Synchronous Condenser and Grid Type SVG in New Energy Power Systems," in *Proc. of 2024 4th International Conference on Electrical Engineering and Control Science (IC2ECS)*, Nanjing, China, Dec. 2024, pp. 30–34.

[36] G. Han, J. Z. Li, and D. F. Cai *et al*., "Impact of a Synchronous Condenser Converted from a Thermal Power Generating Unit on the Voltage Stability of Power System," in *Proc. of 2023 26th International Conference on Electrical Machines and Systems (ICEMS)*, Zhuhai, China, Nov. 2023, pp. 2092–2096.

[37] Y. M. Ma, L. B. Zhou, and J. Wang *et al*., "A New Parameters Identification Method for Novel Synchronous Condenser based on Particle Swarm Algorithm and Wavelet Transform," in *Proc. of 2018 21st International Conference on Electrical Machines and Systems (ICEMS)*, Jeju, Korea (South), Oct. 2018, pp. 593–597.

[38] J. W. Zhao, L. B. Zhou, and J. Wang *et al*., "An Improved Phase Angle Prediction Method for Quasi-synchronous Grid Connection of Large-scale Synchronous Condenser," in *Proc. of 2018 IEEE Student Conference on Electric Machines and Systems*, Huzhou, China, Dec. 2018, pp. 1–4.

[39] L. Hiquiana, J. Sun, and J. Schmall *et al*., "Interactions between Wind Turbines and Synchronous Condensers Equipped with Flywheels," in *Proc. of 2024 9th IEEE Workshop on the Electronic Grid (eGRID)*, Santa Fe, NM, USA, Nov. 2024, pp. 1–6.

[40] Y. K. Zhou, H. D. Sun, and X. L. Wang *et al.*, "Suppressing Overvoltage by Synchronous Condenser based on Multiple Renewable Energy Stations Short Circuit Ratio(MRSCR)," in *Proc. of 2021 IEEE 5th Conference on Energy Internet and Energy System Integration (EI2)*, Taiyuan, China, Oct. 2021, pp. 918–923.

[41] A. D. Wang, Z. M. Zheng, and J. H. Zheng, "Parameter Identification of Synchronous Condenser based on Sensitivity Analysis of Parameters," in *Proc. of 2017 China International Electrical and Energy Conference (CIEEC)*, Beijing, China, Oct. 2017, pp. 725–730.

[42] Y. N. Liu, C. Xia, and G. Q. Yu *et al*., "Synchronous Condenser Fault Diagnosis Method based on RBF Neutral Network," in *Proc. of 2019 IEEE 3rd Conference on Energy Internet and Energy System Integration (EI2)*, Changsha, China, Nov. 2019, pp. 2193–2196.

[43] A. R. Nair, S. Patel, and S. Kamalasadan *et al*., "A State-space based Analysis of Synchronous Condenser Inter-parametric Variations in Wind Integrated Weak Power Grid," in *Proc. of 2022 IEEE Global Conference on Computing, Power and Communication Technologies (GlobConPT)*, New Delhi, India, Sept. 2022, pp. 1–5.

[44] M. Y. Jiang, H. Z. Ma, and Y. D. Lin *et al*., "Stator Interturn Short-circuit Fault Diagnosis in Synchronous Condensers based on the Third Current Harmonic," in *Proc. of 2020 International Conference on Electrical Machines (ICEM)*, Gothenburg, Sweden, Aug. 2020, pp. 1438–1444.

[45] N. Upadhayay, M. Nadarajah, and A. Ghosh, "System Strength Enhancement with Synchronous Condensers for Power Systems with High Penetration of Renewable Energy Generators," in *Proc. of 2021 31st Australasian Universities Power Engineering Conference (AUPEC)*, Perth, Australia, Sept. 2021, pp. 1–5.

[46] V. Gevorgian, P. Koralewicz, and S. Shah *et al*., "Testing GFM and GFL Inverters Operating with Synchronous Condensers," in *Proc. of 2023 IEEE Power & Energy Society General Meeting (PESGM)*, Orlando, FL, USA, Jul. 2023, pp. 1–5.

[47] A. D. Martin, B. Fahimi, and L. N. Tutelea *et al*., "Rotor Current Oriented Control with Efficiency Investigation of a Standalone DFIG with Diode-reactified DC Output," in *Proc. of 2025 International Aegean Conference on Electrical Machines and Power Electronics (ACEMP) & 2025 International Conference on Optimization of Electrical and Electronic Equipment (OPTIM)*, Timisoara, Romania, May 2025, pp. 1–6.

[48] G. R. Xu, Q. W. Li, and H. Wang *et al*., "A New Power Flow Controller based on Dual-excited Synchronous Machine," *IEEE Transactions on Industry Applications*, vol. 61, no. 4, pp. 5880–5890, Jul.-Aug. 2025.

[49] H. H. Xin, K. H. Zhuang, and P. F. Hu *et al*., "Small Signal Synchronization Stability Analysis of Interconnected System Containing Grid-forming and Grid-following Converters from the Perspective of Dual-axis Synchronous Generator," *IEEE Transactions on Energy Conversion*, vol. 40, no. 3, pp. 2520–2534, Sept. 2025.

Prof. Ion Boldea: IEEE member from 1977, IEEE Fellow (1996), Life Fellow since 2011. He received the M.S. and Ph.D. degrees in electrical engineering from the University Politehnica of Timisoara, Timisoara, Romania, in 1967 and 1973, respectively.

He is currently a Full Professor with the University Politehnica of Timisoara, Timisoara. He has authored or coauthored research papers extensively (291 papers, 5395 citation, H index: 40 in Web of Science) in linear and rotary electric machines, drives, and MAGLEVs. He has authored or coauthored numerous books, with 6000 entrances in libraries worldwide (WorldCat.com).

Dr. Boldea was the recipient of the 2015 IEEE Nikola Tesla Award.

Adrian Daniel Martin (IEEE Member '25) received the M.S. and Ph.D. degrees in electrical engineering from the University Politehnica Timisoara, Timisoara, Romania, in 2017 and 2023, respectively.

He is currently a Lecturer at Politehnica University Timisoara, a position he has held since 2024. Additionally, he serves as a MES MOM Automation Senior Analyst at Accenture, Romania, and leads the Student Information and Counseling Office at UPT. His professional background includes a research visiting period at the University of Texas at Dallas in 2024. He has authored numerous scientific papers in Web of Science and IEEE-indexed journals and proceedings. His doctoral research focused on improved induction machine torque observers and virtual loading. His research interests include real-time processing, condition monitoring, torque and electrical parameter analysis in industrial applications, and automation processes.

Dr. Martin actively contributes to the academic community through his teaching, administrative roles, and research in electrical engineering and automation.

Prof. Lucian Nicolae Tutelea (Member, IEEE) received the B.E. and Ph.D. degrees in electrical engineering from the University Politehnica of Timisoara, Timisoara, Romania, in 1989 and 1997, respectively.

He is currently a Professor with the Department of Electric Drives and Power Electronics, University Politehnica Timisoara. He was a Visiting Researcher with the Institute of Energy Technology, Aalborg University, Denmark (1997, 1999, 2000 and 2006); and with the Department of Electrical Engineering, Hanyang University from Seoul, South Korea, in 2004.

Prof. Tutelea main research interests include design, modeling and control of electric machines and drives.